



## Article

# Bandgap Engineering via Doping Strategies for Narrowing the Bandgap below 1.2 eV in Sn/Pb Binary Perovskites: Unveiling the Role of Bi<sup>3+</sup> Incorporation on Different A-Site Compositions

Jeong-Yeon Lee <sup>1</sup>, Seojun Lee <sup>1</sup>, Jun Ryu <sup>1</sup> and Dong-Won Kang <sup>1,2,\*</sup>

<sup>1</sup> Department of Smart Cities, Chung-Ang University, 84 Heukseok-ro, Dongjak-gu, Seoul 06974, Republic of Korea; ekak123@cau.ac.kr (J.-Y.L.); sjlee6758@cau.ac.kr (S.L.); jun2019@cau.ac.kr (J.R.)

<sup>2</sup> Department of Energy Systems Engineering, Chung-Ang University, 84 Heukseok-ro, Dongjak-gu, Seoul 06974, Republic of Korea

\* Correspondence: kangdwn@cau.ac.kr

**Abstract:** The integration of perovskite materials in solar cells has garnered significant attention due to their exceptional photovoltaic properties. However, achieving a bandgap energy below 1.2 eV remains challenging, particularly for applications requiring infrared absorption, such as sub-cells in tandem solar cells and single-junction perovskite solar cells. In this study, we employed a doping strategy to engineer the bandgap and observed that the doping effects varied depending on the A-site cation. Specifically, we investigated the impact of bismuth (Bi<sup>3+</sup>) incorporation into perovskites with different A-site cations, such as cesium (Cs) and methylammonium (MA). Remarkably, Bi<sup>3+</sup> doping in MA-based tin-lead perovskites enabled the fabrication of ultra-narrow bandgap films (~1 eV). Comprehensive characterization, including structural, optical, and electronic analyses, was conducted to elucidate the effects of Bi doping. Notably, 8% Bi-doped Sn-Pb perovskites demonstrated infrared absorption extending up to 1360 nm, an unprecedented range for ABX<sub>3</sub>-type single halide perovskites. This work provides valuable insights into further narrowing the bandgap of halide perovskite materials, which is essential for their effective use in multi-junction tandem solar cell architectures.

**Keywords:** perovskite; bismuth doping; band gap narrowing; composition engineering



**Citation:** Lee, J.-Y.; Lee, S.; Ryu, J.; Kang, D.-W. Bandgap Engineering via Doping Strategies for Narrowing the Bandgap below 1.2 eV in Sn/Pb Binary Perovskites: Unveiling the Role of Bi<sup>3+</sup> Incorporation on Different A-Site Compositions. *Nanomaterials* **2024**, *14*, 1554. <https://doi.org/10.3390/nano14191554>

Academic Editors: Gyaneshwar P. Srivastava, Gang Xiang and Dingyu Yang

Received: 31 August 2024

Revised: 18 September 2024

Accepted: 24 September 2024

Published: 26 September 2024



**Copyright:** © 2024 by the authors. Licensee MDPI, Basel, Switzerland. This article is an open access article distributed under the terms and conditions of the Creative Commons Attribution (CC BY) license (<https://creativecommons.org/licenses/by/4.0/>).

## 1. Introduction

Recent advancements in semiconductor applications for renewable energy have attracted significant attention, particularly in the development of solar cells aimed at addressing the environmental crisis and climate change. The field of halide perovskites within solar cell technology has garnered widespread interest since its initial reports [1–7]. Due to their superior optoelectronic properties, bandgap tunability, and cost-effectiveness, perovskite solar cells have been considered promising alternatives to silicon-based solar cells [8–17]. Over the past decade, the power conversion efficiency (PCE) of perovskite solar cells has rapidly increased, now exceeding 26.1%, which is comparable to that of silicon solar cells [18]. Despite these attractive characteristics, challenges persist in reducing the bandgap to below 1.2 eV, a crucial requirement for their applications in photovoltaic technologies targeting the infrared (IR) spectrum. The lack of narrow-bandgap perovskites capable of absorbing longer-wavelength photons in the IR region up to 1200 nm has led to numerous attempts to achieve this reduction [19–28]. Despite various efforts, the lowest reported bandgap of an ABX<sub>3</sub> perovskite device is approximately 1.2 eV, specifically for MAPb<sub>0.2</sub>Sn<sub>0.8</sub>I<sub>3</sub> perovskite, based on current knowledge [29]. In response, we focused on fabricating perovskites with a bandgap narrower than 1.2 eV. In our previous work, we successfully reduced the bandgap of CsPbI<sub>3</sub> inorganic perovskite by introducing Sn<sup>2+</sup> [30]. Specifically, when Sn<sup>2+</sup> replaced Pb<sup>2+</sup> by 60%, the bandgap decreased from 1.75 eV to

1.35 eV, and phase stability improved compared to CsPbI<sub>3</sub>. However, the phase stability of CsSn<sub>0.6</sub>Pb<sub>0.4</sub>I<sub>3</sub> (CSPI) remained inferior to that of organic cation perovskites, and the bandgap was still higher than desired. To address these challenges, we explored the addition of B-site dopants to CSPI perovskite, as doping is a common and effective strategy to modify perovskite properties. Partial substitution of B-site cations with different metal ions, such as Sr<sup>2+</sup>, Mn<sup>2+</sup>, and Co<sup>2+</sup> has been proposed as a potential method to enhance the phase stability of inorganic perovskites [31–33]. This approach allows tuning of the perovskite structure, surface morphology, crystal size, and photoelectronic properties such as band alignment, charge transport, and defect states. In our research, we specifically focused on the effects of Bi<sup>3+</sup> doping on inorganic perovskites. Bismuth (Bi<sup>3+</sup>) has been widely employed as a dopant in perovskite solar cells due to its similar electron configuration and ionic radius to lead (Pb<sup>2+</sup>) and tin (Sn<sup>2+</sup>), among various heterovalent ions [34–37]. Previous studies have demonstrated the potential benefits of Bi<sup>3+</sup> incorporation in these materials. For example, Hu et al. reported that the incorporation of 4 mol% Bi<sup>3+</sup> could stabilize the  $\alpha$ -phase of CsPbI<sub>3</sub> while simultaneously narrowing the bandgap to 1.56 eV [38]. Similarly, Kajal et al. found that a small amount of Bi<sup>3+</sup> doping stabilized the distorted  $\beta$ -phase of CsPbI<sub>3</sub> perovskite and slightly red-shifted the photoluminescence (PL) peak towards a higher wavelength [39]. Wang et al. observed that substituting Sn<sup>2+</sup> with Bi<sup>3+</sup> enhanced the crystallinity of CsSnI<sub>3</sub> perovskite [40]. Lee et al. reported that doping 3 mol% of Bi<sup>3+</sup> into CsSnI<sub>3</sub> perovskite improved the stability of the B- $\gamma$  phase and shifted the absorption onset to a longer wavelength [41]. These intriguing results inspired us to explore the application of Bi<sup>3+</sup> doping in our research.

In this study, we incorporated Bi<sup>3+</sup> into an inorganic, tin-lead (Sn-Pb) binary perovskite system, specifically focusing on CSPI, to explore the potential of Bi<sup>3+</sup> doping in enhancing stability and tuning the bandgap of these materials. We further compared the effects of Bi<sup>3+</sup> doping on cesium (Cs)-based and MA-based, tin-lead perovskites to understand how the A-site cation in the ABX<sub>3</sub> perovskite structure influences these properties. Our results demonstrated that Bi<sup>3+</sup> doping adversely impacted the crystallinity and disrupted the crystal structure of CSPI. Conversely, in MA-based, tin-lead perovskites, the crystal structure remained intact after Bi<sup>3+</sup> doping, and a significant red-shift in the absorption onset was observed. Additionally, the bandgap of MA-based, tin-lead perovskites decreased progressively with increasing Bi<sup>3+</sup> concentration. This study provides insight into the effects of Bi<sup>3+</sup> doping on the excitonic properties, structural phases, and surface morphology of different A-site, tin-lead perovskites, highlighting the potential of Bi-doped, MA-based perovskites for extended photoresponse applications in the infrared (IR) region, up to 1360 nm.

## 2. Materials and Methods

### 2.1. Materials

Cesium iodide (CsI, 99.999%, Alfa Aesar, Incheon, Republic of Korea), Methylammonium iodide (MAI, 99.99%, Greatcell Solar, Queanbeyan, Australia) Lead(II) iodide (PbI<sub>2</sub>, 99.99%, Tokyo Chemical Industry Co., Ltd., Tokyo, Japan), Tin(II) iodide (SnI<sub>2</sub>, 99.99% Sigma-Aldrich, Saint Louis, MO, USA), tin(II) fluoride (SnF<sub>2</sub>, 99%, Sigma-Aldrich), were purchased and used as precursors for Sn-Pb binary perovskites. Dimethylformamide (DMF, 99.5%, Samchun Chemical, Seoul, Republic of Korea) and dimethyl sulfoxide (DMSO, 99.8%, Samchun Chemical), toluene (99.8%, Samchun Chemical), 2-Propanol (IPA, 99.99%, Sigma-Aldrich), and chlorobenzene (CBZ, 99%—GR grade, Wako, Richmond, VA, USA) were used as solvents. Acetone ( $\geq 99\%$ , Samchun Chemical) and Isopropanol (IPA,  $\geq 99.5\%$ , Samchun Chemical) were used as cleaning solvents for Indium-doped tin oxide (ITO)-coated glasses (ITO, 10  $\Omega$  sq<sup>−1</sup>, AMG). Poly(3,4-ethylenedioxythiophene) polystyrenesulfonate (PEDOT:PSS, PVP AI 4083) was sourced from Clevios™ (Leverkusen, Germany). Phenyl-C61-butyric acid methyl ester (PC<sub>61</sub>BM, 99.5%) was sourced from Organic Semiconductor Materials (OSM, Seoul, Republic of Korea) and Bathocuproin (BCP, 98%) was purchased

from Alfa Aesar. Silver pellet (Ag pellet, 99.99%, RND Korea, Seoul, Republic of Korea) was used as the electrode by thermal evaporator.

## 2.2. Preparation of Perovskite Precursors

A Cs-based:  $\text{CsSn}_{0.6}\text{Pb}_{0.4}\text{I}_3$  precursor was prepared from CsI,  $\text{PbI}_2$ ,  $\text{SnI}_2$  with 0.5 M concentration (the stoichiometric ratio of  $\text{CsI}:\text{SnI}_2:\text{PbI}_2$  is 1:0.6:0.4), excess  $\text{SnF}_2$  of 0.03 M, as an additive. Then,  $\text{BiI}_3$  of 0.005 M was added for Bi-doped Sn-Pb perovskite. After that, a DMF- and DMSO-mixed solvent (the ratio of DMF and DMSO is 0.8:0.2) was added to the prepared bottle of 1 mL. The Cs-based Sn-Pb perovskite solution was completely prepared after stirring for 2 h.

A MA-based:  $\text{MASn}_{0.6}\text{Pb}_{0.4}\text{I}_3$  precursor was prepared from MAI,  $\text{PbI}_2$ , and  $\text{SnI}_2$  with 1 M concentration (the stoichiometric ratio of  $\text{MAI}:\text{SnI}_2:\text{PbI}_2$  is 1:0.6:0.4), excess  $\text{SnF}_2$  of 0.06 M, as an additive.  $\text{BiI}_3$  of 0.01, 0.02, 0.04, 0.08 M is added for Bi-doped Sn-Pb perovskite. After that, a DMF- and DMSO-mixed solvent (the ratio of DMF and DMSO is 0.8:0.2) of 1 mL was added to the prepared bottle. The MA-based, Sn-Pb perovskite solution was completely prepared after stirring for 2 h.

## 2.3. Fabrication of Tin-Lead Perovskite Thin Films and Devices

ITO-coated glasses were sequentially cleaned with acetone and IPA in the ultrasonic bath for 20 min, respectively. After cleaning, the glass substrates were dried in the dry oven at 95 °C to evaporate residual solvents. The cleaned substrates were then subjected to a UV treatment for 30 min. PEDOT:PSS was spin-coated onto the ITO substrates at 5000 rpm for 30 s in ambient conditions and annealed at 150 °C for 20 min on a hotplate as a hole transport layer (HTL) (thickness is ca. 20–30 nm). Then, the HTL-coated substrates were transferred to a  $\text{N}_2$ -filled glove box. The Cs-based perovskite precursor solutions, with or without  $\text{Bi}^{3+}$ , were spin-coated at 5000 rpm for 60 s on top of the HTL film and annealed at 80 °C for 30 min on a hot plate. The MA-based perovskite precursor solutions, with or without  $\text{Bi}^{3+}$ , were spin-coated at 5000 rpm for total of 35 s (acceleration time: 5 s) in the  $\text{N}_2$ -filled glove box. A 300  $\mu\text{L}$  of toluene was applied dropwise in the center of the MA-based perovskite film at 12–13 s during the spin coating. The MA-based perovskite-coated substrate was annealed at 80 °C 10 min. For an electron transport layer, a  $\text{PC}_{61}\text{BM}$  solution with 20  $\text{mg mL}^{-1}$  dissolved in CBZ was spin-coated onto the perovskite film at 1500 rpm for 35 s and annealed at 80 °C for 10 min. A BCP solution (0.5  $\text{mg mL}^{-1}$  dissolved in IPA) was spin-coated at 5000 rpm for 20 s and annealed at 80 °C for 5 min. The silver top electrodes (ca. 180 nm) were thermally evaporated under a high vacuum condition ( $<2 \times 10^{-6}$  Torr) with a shadow mask (the size of each solar cell device is 4  $\text{mm}^2$ ).

## 2.4. Characterizations

The optical absorption spectra were characterized using ultraviolet-visible (UV-Vis-Nir) spectroscopy (UV-2700, Shimadzu). Prior to scanning the perovskite samples, baseline correction was performed within a scan range of 300–1400 nm. The crystal structure of the perovskite films was evaluated via X-ray diffraction (XRD) (D8-Advance, Bruker-AXS). The XRD data were recorded in the two-theta range from 10° to 60°, with a scanning rate of 1°  $\text{min}^{-1}$ , at room temperature (RT). The measurement conditions included a scan speed of 100 nm/min and an interval step size of 1 nm. The surface morphologies and cross-sectional images were investigated by field emission scanning electron microscopy (FE-SEM; AURIGA, Carl Zeiss). Steady-state photoluminescence (PL) spectra were acquired using a spectrofluorometer (Fluorolog3 with TCSPC, HORIBA SCIENTIFIC) with laser excitation at 463 nm.

All device characterizations were conducted under ambient conditions (RT and relative humidity of 25–30%). J-V curves of the perovskite solar cells were measured using a solar simulator (PEC-L01, Peccell Technologies) under standard AM1.5 illumination (power: 100  $\text{mW cm}^{-2}$ ). EQE spectra were characterized using a CompactStat instrument (Ivium Technologies; Eindhoven, The Netherlands), which includes a power source

(Abet Technologies 150 W xenon lamp, 13014) and a monochromator (DongWoo Opteron, MonoRa500i).

### 3. Results

Figure 1 presents the fundamental characterization of the absorption spectra and XRD patterns for pristine and Bi-doped CSPI perovskite films. As seen in the absorption spectra (Figure 1a), the absorbance profiles of the pristine and Bi-doped CSPI films were nearly identical. To provide greater clarity, an enlarged spectral range from 700 nm to 1200 nm is included in the inset of Figure 1a. A FE-SEM confirmed that all films had a comparable thickness of  $170 \pm 10$  nm, ensuring that variations in film thickness did not contribute to the observed absorption differences. The absorption onset for Bi-doped samples exhibited a slight blue shift, indicating a modest increase in the bandgap. According to Tauc's law, the absorption coefficient ( $\alpha$ ) is related to the bandgap energy ( $E_g$ ), as follows [42]:

$$\alpha h\nu = \beta(h\nu - E_g)^n$$

where  $\beta$  is a constant independent of photon energy, and  $E_g$  represents the optical bandgap. The parameter  $n$  characterizes the transition process, with  $n = \frac{1}{2}$  for allowed direct transitions and  $n = 2$  for allowed indirect transitions. Figures 1b and 2b present the Tauc plots obtained using the above equation given direct transitions. The  $E_g$  value for the films was determined by extrapolating the linear portion of this relationship to its intersection with the abscissa (where  $\alpha = 0$ ,  $E_g = h\nu$ ). The bandgap was found to be 1.32 eV for pristine CSPI and 1.33 eV for Bi-doped CSPI. An XRD analysis (Figure 1c,d) confirmed the crystal phase of both pristine and Bi-doped CSPI perovskites. Despite the similar absorption properties post-Bi doping, significant changes were observed in the XRD patterns.

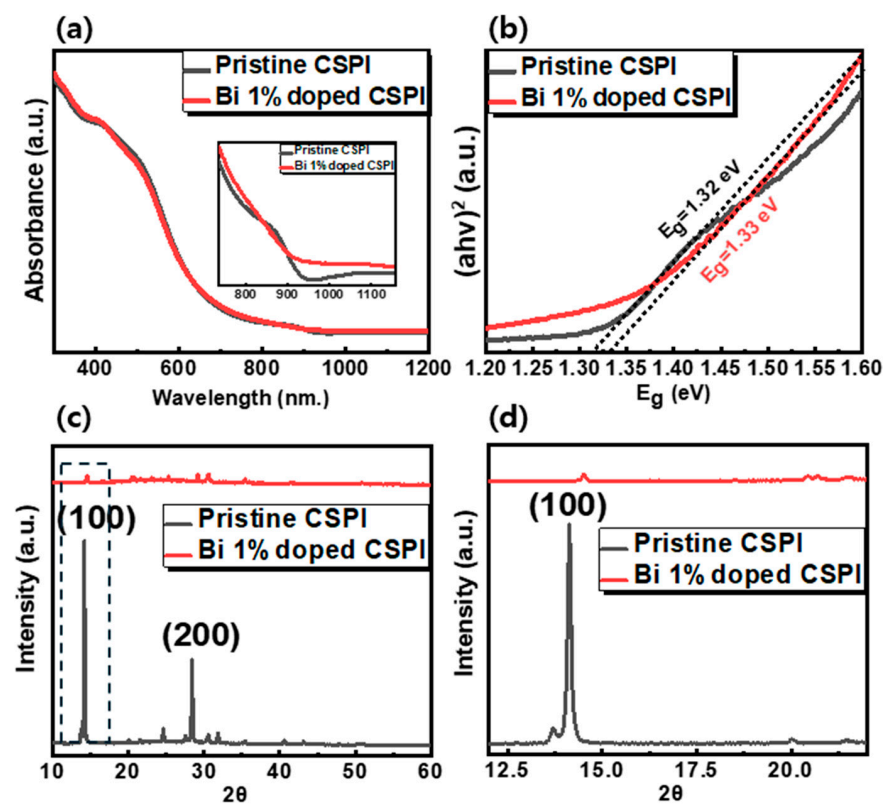


**Figure 1.** (a) Absorption spectra of pristine and Bi 1% doped CSPI perovskite films, with the inset highlighting the enlarged absorption spectrum, (b) Tauc plot of pristine and Bi 1% doped CSPI perovskite films, (c) Stacked XRD patterns of pristine and Bi 1% doped CSPI perovskite films with dashed box highlighting the main peak, (d) Main XRD peak of pristine and Bi 1% doped CSPI perovskite films.

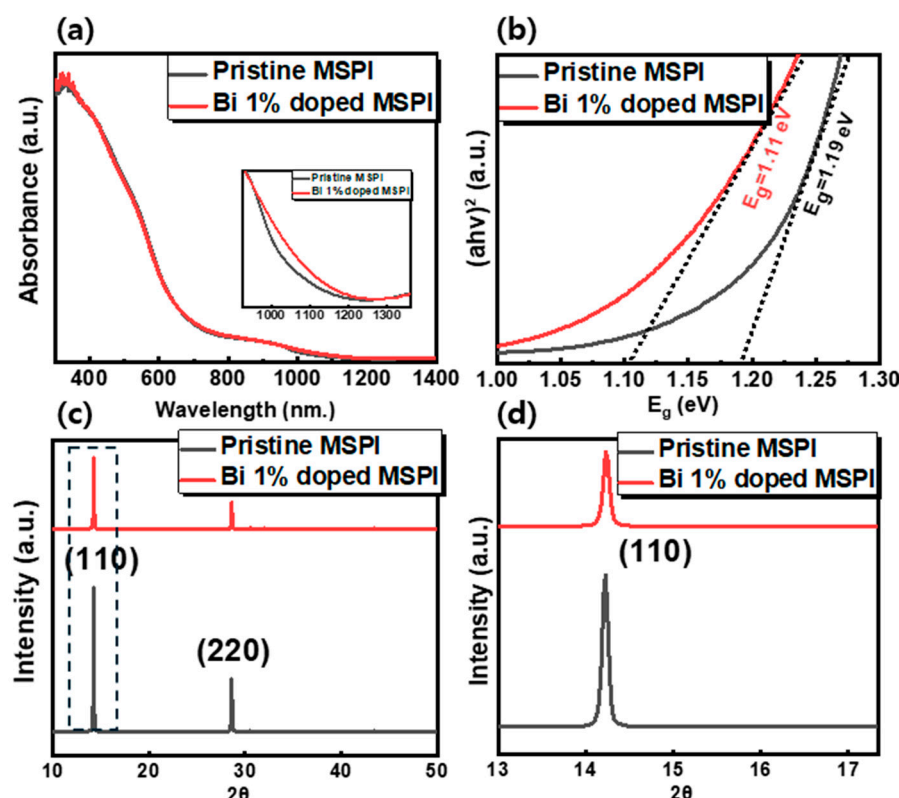


**Figure 2.** (a) Absorption spectra of pristine and Bi 1% doped MSPI perovskite films, with the inset highlighting the enlarged absorption spectrum, (b) Tauc plot of pristine and Bi 1% doped MSPI perovskite films, (c) Stacked XRD patterns of pristine and Bi 1% doped MSPI perovskite films with dashed box highlighting the main peak, (d) Main XRD peak of pristine and Bi 1% doped MSPI perovskite films.

The XRD peaks of Bi-doped CSPI were notably different from those of pristine CSPI perovskite. As shown in Figure S1, the XRD pattern for Bi-doped samples revealed several new peaks correspond to  $\text{Cs}_3\text{Bi}_2\text{I}_9$ ,  $\text{Cs}_2\text{SnI}_6$  and tetragonal  $\text{CsSnI}_3$ . This suggests that the incorporation of  $\text{Bi}^{3+}$  to CSPI disrupted the original structure, leading to the formation of secondary phases such as  $\text{Cs}_3\text{Bi}_2\text{I}_9$ . Previous studies have reported that  $\text{Cs}_3\text{Bi}_2\text{I}_9$  has a bandgap of 1.9–2.2 eV [43–45],  $\text{CsSnI}_3$  has a bandgap of 1.85–2.49 eV [46,47], and  $\text{Cs}_2\text{SnI}_6$  has a bandgap of 1.27–1.62 eV [48–50]. Given that the bandgaps of these decomposition phases are higher than that of CSPI, the observed bandgap increases might be due to the secondary phases. Additionally, the XRD peak intensities for Bi-doped CSPI were significantly reduced compared to those of the pristine CSPI, indicating a decrease in crystallinity.

Given that Bi-doping negatively affected the structural phase and did not reduce the bandgap of CSPI, we substituted Cs with MA at the A-site to check the effects of A-site cation in the  $\text{ABX}_3$  architecture on its photophysical characteristics. Interestingly, the bandgap decreased further as the MA content increased. Figure S2a presents the absorption spectra of pristine and Bi-doped  $\text{Cs}_{0.5}\text{MA}_{0.5}\text{Sn}_{0.6}\text{Pb}_{0.4}\text{I}_3$  ( $\text{Cs}_{0.5}\text{MA}_{0.5}\text{SPI}$ ) perovskites. For clear analysis, the graph was magnified (as shown in the inset), revealing a slight red-shift in the absorption onset towards longer wavelengths. The bandgaps were determined using the Tauc plot to be 1.23 eV and 1.2 eV for pristine and Bi-doped  $\text{Cs}_{0.5}\text{MA}_{0.5}\text{SPI}$  perovskites, respectively (Figure S2b). To further validate the bandgap trend with increasing MA substitution for Cs, a MA-dominant composition ( $\text{Cs}_{0.25}\text{MA}_{0.75}$ ) was also examined. Figure S2c shows the absorption spectra of pristine and Bi-doped  $\text{Cs}_{0.25}\text{MA}_{0.75}\text{Sn}_{0.6}\text{Pb}_{0.4}\text{I}_3$  ( $\text{Cs}_{0.25}\text{MA}_{0.75}\text{SPI}$ ) perovskites. Upon closer inspection at higher magnification, a red-shift in the bandgap toward the longer wavelength region is evident, as depicted in the inset of Figure 2c. From the Tauc plot in Figure S2d, the bandgaps of pristine and Bi-doped



$\text{Cs}_{0.25}\text{MA}_{0.75}\text{SPI}$  were determined to be 1.2 eV and 1.14 eV, respectively. The bandgap decrement is greater in Bi-doped  $\text{Cs}_{0.25}\text{MA}_{0.75}\text{SPI}$  than in Bi-doped  $\text{Cs}_{0.5}\text{MA}_{0.5}\text{SPI}$  perovskites, suggesting that bismuth tends to act as a dopant that reduces the bandgap more effectively in MA-dominant perovskites than in Cs-based perovskites. This observation led us to further investigate the complete substitution of Cs with MA. Surprisingly, when the same characterizations were applied to pristine and Bi-doped  $\text{MASn}_{0.6}\text{Pb}_{0.4}\text{I}_3$  (MSPI), the results differed from those of CSPI perovskites. Figure 2a illustrates the absorption spectra of pristine and Bi-doped MSPI films. At a lower magnification, the graphs appeared nearly identical; however, as shown in the inset of Figure 2a, the extended spectral range from 900 nm to 1400 nm revealed a significant red-shift in the absorption onset towards longer wavelengths. The FE-SEM measurements confirmed that all films had a comparable thickness of  $350 \pm 10$  nm, ruling out any influence of film thickness on the observed absorption differences. According to the Tauc plot analysis (Figure 2b), the bandgap was estimated to be 1.19 eV for pristine MSPI and 1.11 eV for Bi-doped MSPI. This substantial reduction in bandgap prompted further exploration by increasing  $\text{Bi}^{3+}$  concentrations. Figure S3 displays the absorption spectra and Tauc plot for MSPI with varying Bi-doping ratios. Notably, the absorption onset gradually shifted towards longer wavelengths with increasing doping concentration, as shown in Figure S3a. A clear reduction in the bandgap was observed from the Tauc plot (Figure S3b), with the bandgap reaching 1.055 eV for 8% Bi-doped MSPI. This significant extension of the absorption range following Bi-doping is consistent with reports on other MA-based perovskites such as  $\text{MAPbCl}_3$ ,  $\text{MAPbBr}_3$ , and  $\text{MAPbI}_3$ . Zhang et al. observed a considerable red-shift in the absorption onset with increasing  $\text{Bi}^{3+}$  content in  $\text{MAPbCl}_3$  single crystals [51]. The minimum bandgap of 2.62 eV was obtained for Bi-doped  $\text{MAPbCl}_3$ , which is 300 meV narrower than that of pristine  $\text{MAPbCl}_3$  (2.92 eV). By combining theoretical calculations with experimental results, they speculated that the energy level of the empty 6p orbitals of  $\text{Bi}^{3+}$  is lower than that of  $\text{Pb}^{2+}$ . Thus, with increasing  $\text{Bi}^{3+}$  content, the conduction band minimum (CBM) shifts downward, narrowing the bandgap. Similarly, Abdelhady et al. found that the absorption spectra displayed a red-shift proportional to the  $\text{Bi}^{3+}$  content in  $\text{MAPbBr}_3$  crystals [52]. Based on density functional theory (DFT) calculations, they suggested that the relatively shallow and delocalized  $\text{Bi}^{3+}$  states facilitate interactions between nearby  $\text{Bi}^{3+}$  dopants, creating conditions conducive to bandgap narrowing. Likewise, Wang et al. used  $\text{Bi}^{3+}$  as a dopant in  $\text{MAPbI}_3$  perovskite and observed a red-shift of 140 meV in the absorption onset [53]. They proposed that the bandgap reduction could be attributed to the creation of impurity bands within the bandgap. Due to their similar electron configurations and ionic radii,  $\text{Bi}^{3+}$  ions can be incorporated into the crystal lattice of lead perovskites, generating  $\text{Bi}_{\text{Pb}}$  defects that act as shallow donors and introduce energy levels below the CBM. Therefore, we proceeded with the fabrication of devices for Bi-doped  $\text{MAPbI}_3$  perovskites to verify the bandgap change, as detailed in the following sections. The crystal phases of pristine and Bi-doped  $\text{MAPbI}_3$  perovskites were confirmed by XRD measurements. The XRD pattern (Figure 2c,d) shows the characteristic tetragonal phase structure at room temperature, with main diffraction peaks at  $2\theta$  values of  $14^\circ$  and  $28^\circ$ . The diffraction pattern for Bi-doped perovskite films did not reveal any new peaks and was largely consistent with that of pristine MSPI perovskites. Although the peak intensity for Bi-doped samples was lower than that of the pristine samples, the crystal phase was better preserved compared to Bi-doped CSPI perovskite. Table 1 compares the band gap and crystallographic parameters of CSPI perovskite films with those of MSPI perovskite films.

**Table 1.** Comparison of bandgap and crystallographic parameters for pristine and Bi-doped CSPI and MSPI perovskite films.

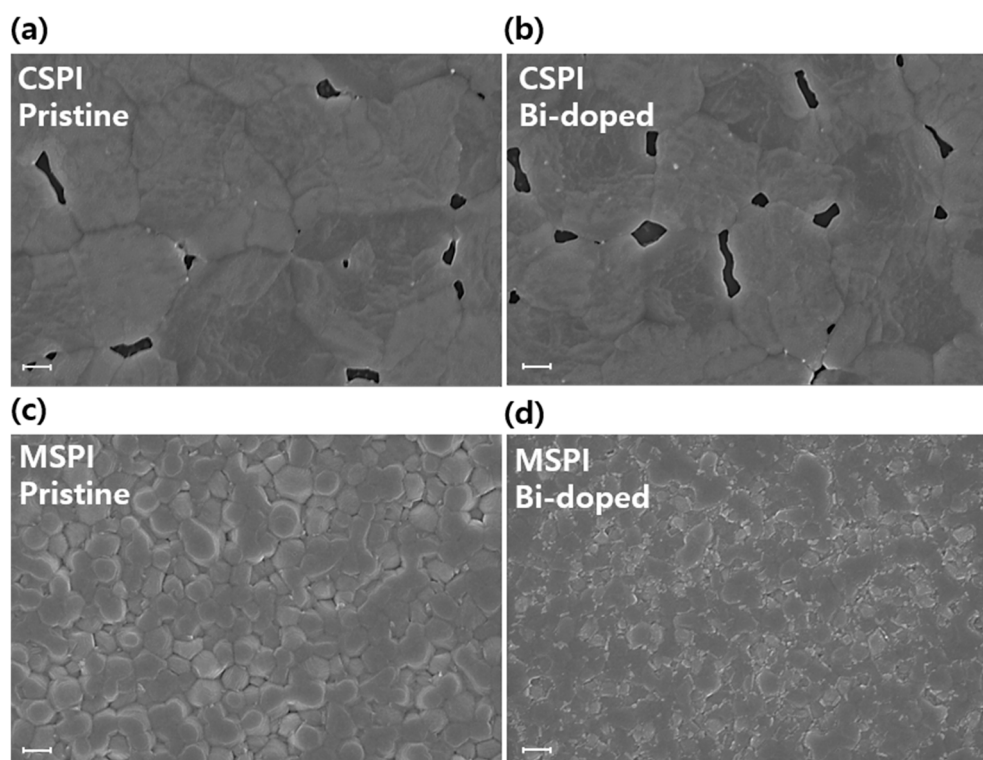
	Bi <sup>3+</sup> Concentration [%]	Band Gap [eV]	Lattice Parameter [Å]	Crystallite Size [nm]
CSPI	0	1.32	6.27	78.34
	1	1.33	6.10	66.38
MSPI	0	1.19	6.21	86.08
	1	1.11	6.22	77.13

Figure 3 presents the surface FE-SEM images of pristine and Bi-doped CSPI and MSPI perovskite thin films. As shown in Figure 3a,b, the Bi-doped CSPI perovskite thin film exhibits more pinholes and a smaller grain size compared to the pristine film. In contrast, the surface morphology of the Bi-doped MSPI perovskite thin film (Figure 3c,d) closely resembles that of the pristine film. The pristine MSPI perovskite thin film displays distinct grain domains of approximately 300 nm and a pinhole-free, homogeneous surface. The Bi-doped MSPI perovskite thin film also shows a pinhole-free surface, albeit with slightly smaller and less uniform grain sizes compared to the pristine film. Despite the somewhat degraded surface quality of the Bi-doped MSPI perovskite thin film, the overall morphology remains relatively uniform and compact. These contrasting outcomes align with the structural analysis trends. As previously mentioned, the inherent phase instability of CSPI, due to its small tolerance factor (Table S1), prevents it from maintaining its original structure. The XRD measurements revealed that Bi-doping led to the decomposition of the CSPI structure into several phases. Consequently, Bi incorporation into the CSPI perovskite negatively impacted crystal growth, which is reflected in the morphological properties. After SEM analyses, energy dispersive X-ray spectroscopy (EDS) was performed to determine the elemental composition of pristine and 8% Bi-doped MSPI perovskites (Figure S4). The specific atomic percentages and the Sn/Pb ratio are provided in the inset table. Since tin(II) fluoride (SnF<sub>2</sub>) was added to suppress the oxidation of Sn<sup>2+</sup> to Sn<sup>4+</sup>, and due to its surface accumulation properties, the Sn content might be detected to be over 60% in all samples. Additionally, the Bi content in the thin films of Bi-doped MSPI perovskite was lower than the nominal Bi content in the precursor solutions, consistent with previous reports on Bi-doped FAPbI<sub>3</sub> [37]. According to the EDS results, the Sn/Pb ratio decreased from 1.92 to 1.83 after Bi-incorporation, indicating that Sn might be mainly replaced by Bi. Prior reports, supported by density functional theory (DFT) calculations, have shown that the formation energy of Bi<sub>Sn</sub> is lower than that of Bi<sub>Pb</sub>, suggesting a higher likelihood of Sn substitution by Bi compared to Pb. Furthermore, the ionic radius of Bi<sup>3+</sup> (1.03 Å) is closer to that of Sn<sup>2+</sup> (1.04 Å) than to Pb<sup>2+</sup> (1.19 Å) [54], making Sn replacement by Bi more probable in this structure.

Given that surface quality significantly influences device performance, only MA-based perovskites were further developed for device fabrication.

To assess the impact of Bi-doping on solar cell performance, devices were fabricated using pristine and Bi-doped MSPI perovskites as the light-absorbing layer. The preparation process for these devices is depicted in Figure 4a. The J-V curves (Figure S5a) for both device types indicate a significant degradation in the photovoltaic performance of Bi-doped MSPI perovskite devices. A notable decrease in open-circuit voltage (V<sub>oc</sub>) was observed, corresponding to a sharp reduction in PL intensity (Figure S5b). This substantial PL quenching was also observed in Bi-doped MAPbI<sub>3</sub> and CsSnI<sub>3</sub> perovskites [41,53]. It was confirmed that Bi<sup>3+</sup> incorporation generates Bi<sub>Pb</sub> defects, which act as shallow donors and introduce energy levels below the conduction band minimum (CBM) in MAPbI<sub>3</sub> perovskites. Similarly, the decrease in PL intensity of Bi-doped CsSnI<sub>3</sub> perovskites can be attributed to the formation of intermediate bands below the conduction band due to the BiI<sub>3</sub> doping. Therefore, the PL decrease can be explained by the enhanced non-radiative recombination, as carriers are trapped in the intermediate energy bands introduced by

bismuth. Moreover, the  $V_{oc}$  loss is also likely due to the defect states introduced by  $Bi^{3+}$  and reduced grain size and increased grain boundaries within the bulk material. Additionally, the short-circuit current density ( $J_{sc}$ ) exhibited a more pronounced decline than  $V_{oc}$ , dropping from  $24.73 \text{ mA cm}^{-2}$  to approximately  $0.3\text{--}0.4 \text{ mA cm}^{-2}$  after Bi-doping. This drastic reduction in  $J_{sc}$  is consistent with the earlier explanation for the bandgap decrease. Although light absorption is a key factor influencing short-circuit current, UV-Vis measurements demonstrated that increased Bi concentration did not affect light absorption. The loss in  $J_{sc}$  may instead be attributed to increased bulk recombination, leading to reduced charge extraction. This increase in bulk recombination could result from strong doping of the perovskite bulk or the presence of space charges caused by filled traps or accumulated ionic species. Furthermore, as indicated by the FE-SEM images, the deteriorated surface morphology and increased grain boundaries in the Bi-doped MSPI thin film could serve as trap sites, facilitating charge capture and further reducing short-circuit currents. Interestingly, a progressive decline in performance was observed in proportion to the  $Bi^{3+}$  concentration, as shown in Figure 4b. The photovoltaic performance factors are summarized in Table 2.



**Figure 3.** (a) Surface FE-SEM image of pristine CSPI perovskite film on a glass substrate, (b) Surface FE-SEM image of Bi-doped CSPI perovskite film on a glass substrate, (c) Surface FE-SEM image of pristine MSPI perovskite film on a glass substrate, (d) Surface FE-SEM image of Bi-doped MSPI perovskite film on a glass substrate. Scale bar: 300 nm.

**Table 2.** Photovoltaic Performance Factors for Pristine and Bi-doped MSPI Perovskite Devices.

Bi Concentration [%]	$V_{oc}$ [V]	$J_{sc}$ [ $\text{mA cm}^{-2}$ ]	FF [%]	PCE [%]
0	0.656	24.73	73.58	11.95
1	0.2501	0.375	62.0258	0.0582
2	0.2122	0.3	60.07	0.0383
4	0.197	0.225	57.24	0.0254
8	0.155	0.175	50.69	0.0138



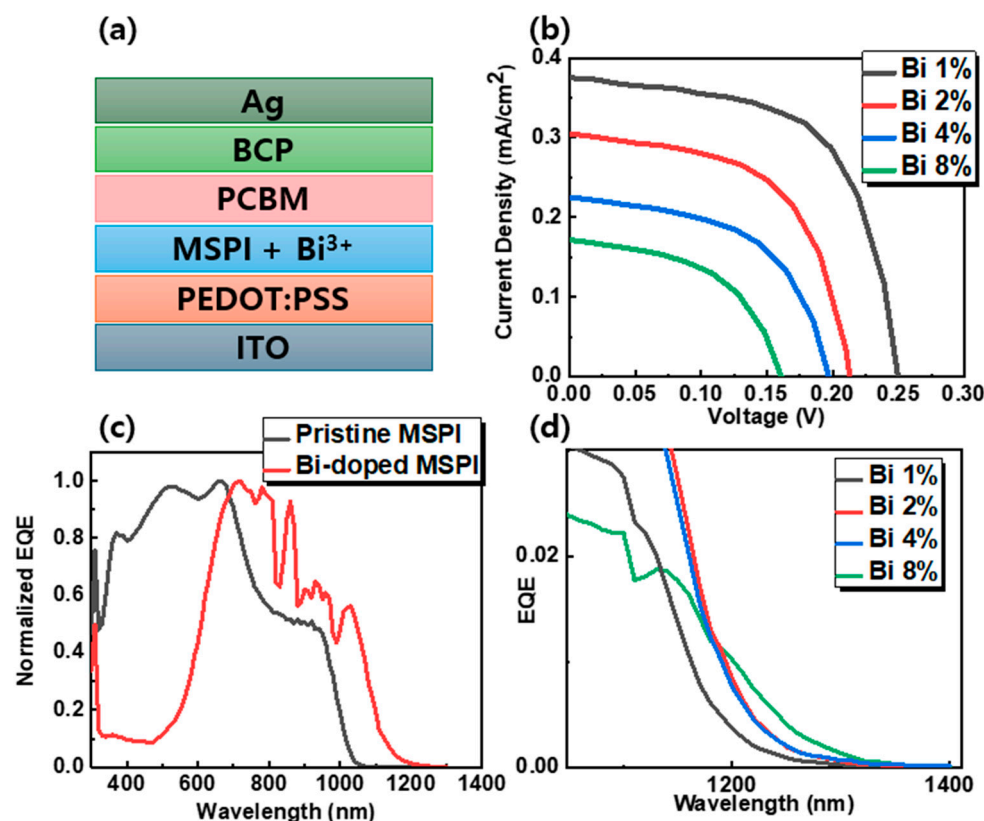


**Figure 4.** (a) Device configuration diagram, (b) J-V curves of 1%, 2%, 4%, and 8% Bi-doped MSPI devices, (c) Normalized EQE spectrum of pristine and Bi 1% doped MA-based devices, (d) Enlarged EQE spectrum of 1%, 2%, 4%, and 8% Bi-doped MSPI devices.

To further understand the effect of Bi-doping on charge carrier diffusion, the EQE of the devices was measured, as shown in Figure 4c,d. From the normalized EQE, it was observed that the NIR charge collection was significantly enhanced when Bi was incorporated. This result is consistent with the absorption measurements in Figure 2a and Figure S3a. As shown in Figure S6, the EQE sharply decreased for Bi-doped devices, confirming the poor performance previously noted. This suggests that Bi<sup>3+</sup> incorporation creates trap sites in the thin film, reducing carrier collection efficiency. Additionally, this performance degradation could stem from reduced charge carrier mobility, caused by increased asymmetric carrier trapping at grain boundaries and shorter charge carrier lifetimes due to diminished intrinsic electronic quality. Nonetheless, a clear red-shift in the onset of the normalized EQE spectrum was observed following Bi-doping. Figure 4c illustrates that the Bi-doped solar cells collected longer-wavelength spectra more effectively than the pristine cells, extending the device response from 1060 nm in the pristine state to 1260 nm in cells doped with 1% Bi. As shown in Figure 4d, the EQE response continued to extend with increasing Bi concentration, reaching an operational wavelength of up to 1360 nm in 8% Bi-doped MSPI. This unprecedented extension of the operational range confirms that Bi-doping enhances the photoresponse of MSPI perovskites, as evidenced by both absorption and EQE measurements. It is deemed necessary to address the technical issues related to the defects currently observed by developing additional compositions and additive processes. Nevertheless, this study has identified the lowest bandgap (~1360 nm, 1.055 eV) that can be achieved in a single halide perovskite with an ABX<sub>3</sub> structure, which is quite significant. With further research, new materials that strongly absorb near-infrared bands and suppress defect formation could dominate next-generation perovskite technology and potentially challenge solar cells based on III-V compounds.

#### 4. Conclusions

This study presents the first development of Bi-doped CSPI tin-lead binary perovskite, inspired by prior reports indicating enhanced phase stability and reduced bandgap in Bi-doped unary perovskites. Contrary to expectations, Bi<sup>3+</sup> incorporation into CSPI adversely affected the structure, leading to the formation of secondary decomposition phases and an unexpected increase in the bandgap. Additionally, surface morphology deteriorated. However, when the A-site cation was switched from Cs to MA, significant improvements were observed, highlighting the critical importance of A-site selection in doping strategies. While Bi<sup>3+</sup> incorporation led to some deterioration in photovoltaic properties, it successfully reduced the bandgap of MSPI perovskite by more than 0.1 eV, achieving an unprecedented narrow bandgap of 1.055 eV in solution-processed halide perovskite films. This is a significant advancement, as current research on perovskites with bandgaps below 1.2 eV is limited. Despite performance challenges, Bi<sup>3+</sup> doping remains a promising approach for developing super-narrow bandgap perovskite solar cells with extended infrared photo-response up to ~1400 nm. Further investigation into the underlying mechanisms of Bi<sup>3+</sup> incorporation based on A-site composition will be crucial for advancing bandgap engineering strategies in ultra-narrow bandgap perovskites.

**Supplementary Materials:** The following supporting information can be downloaded at: <https://www.mdpi.com/article/10.3390/nano14191554/s1>, Figure S1: (a) XRD patterns of Bi-doped CSPI perovskites along with simulated patterns for CsSnI<sub>3</sub>, Cs<sub>2</sub>SnI<sub>6</sub>, and Cs<sub>3</sub>Bi<sub>2</sub>I<sub>9</sub>; Figure S2: (a) Absorption spectra of pristine and Bi-doped Cs<sub>0.5</sub>MA<sub>0.5</sub>SPI perovskite films, with the inset highlighting the enlarged absorption spectrum, (b) Tauc plot of pristine and Bi-doped Cs<sub>0.5</sub>MA<sub>0.5</sub>SPI perovskite films, (c) Absorption spectra of pristine and Bi-doped Cs<sub>0.25</sub>MA<sub>0.75</sub>SPI perovskite films, with the inset highlighting the enlarged absorption spectrum, (d) Tauc plot of pristine and Bi-doped Cs<sub>0.25</sub>MA<sub>0.75</sub>SPI perovskite films; Figure S3: (a) Absorption spectra of pristine and Bi-doped (1%, 2%, 4%, 8%) MSPI perovskite films, (b) Tauc plots for pristine and Bi-doped (1%, 2%, 4%, 8%) MSPI perovskite films; Table S1: Bismuth concentration and tolerance factor of pristine and Bi-doped CSPI and MSPI perovskite films; Figure S4: (a) EDS results of pristine MSPI and (b) Bi-doped MSPI perovskite films; Figure S5: (a) J-V curves of pristine and Bi-doped MSPI perovskite devices, (b) Steady-state PL spectra of pristine and Bi-doped MSPI perovskite devices; Figure S6: (a) EQE spectra of pristine and Bi-doped MSPI devices.

**Author Contributions:** Conceptualization, J.-Y.L.; Data curation, J.R.; Funding acquisition, D.-W.K.; Methodology, S.L.; Resources, S.L.; Supervision, D.-W.K.; Validation, J.R.; Writing—original draft, J.-Y.L. All authors have read and agreed to the published version of the manuscript.

**Funding:** This research was funded by the National Research Foundation of Korea (NRF) funded by the Korea government (MSIT) (RS-2023-00217270, RS-2023-00212744) and also supported by the Chung-Ang University Research Scholarship Grants in 2023.

**Data Availability Statement:** The original contributions presented in the study are included in the article/Supplementary Materials, further inquiries can be directed to the corresponding author.

**Conflicts of Interest:** The authors declare no conflicts of interest.

#### References

1. Kojima, A.; Teshima, K.; Shirai, Y.; Miyasaka, T. Organometal halide perovskites as visible-light sensitizers for photovoltaic cells. *J. Am. Chem. Soc.* **2009**, *131*, 6050–6051. [[CrossRef](#)] [[PubMed](#)]
2. Park, J.; Kim, J.; Yun, H.-S.; Paik, M.J.; Noh, E.; Mun, H.J.; Kim, M.G.; Shin, T.J.; Seok, S.I. Controlled growth of perovskite layers with volatile alkylammonium chlorides. *Nature* **2023**, *616*, 724–730. [[CrossRef](#)] [[PubMed](#)]
3. Liu, M.; Johnston, M.B.; Snaith, H.J. Efficient planar heterojunction perovskite solar cells by vapour deposition. *Nature* **2013**, *501*, 395–398. [[CrossRef](#)] [[PubMed](#)]
4. Burschka, J.; Pellet, N.; Moon, S.-J.; Humphry-Baker, R.; Gao, P.; Nazeeruddin, M.K.; Grätzel, M. Sequential deposition as a route to high-performance perovskite-sensitized solar cells. *Nature* **2013**, *499*, 316–319. [[CrossRef](#)] [[PubMed](#)]
5. Nie, W.; Tsai, H.; Asadpour, R.; Blancon, J.-C.; Neukirch, A.J.; Gupta, G.; Crochet, J.J.; Chhowalla, M.; Tretiak, S.; Alam, M.A. High-efficiency solution-processed perovskite solar cells with millimeter-scale grains. *Science* **2015**, *347*, 522–525. [[CrossRef](#)]

6. Jeon, N.J.; Noh, J.H.; Yang, W.S.; Kim, Y.C.; Ryu, S.; Seo, J.; Seok, S.I. Compositional engineering of perovskite materials for high-performance solar cells. *Nature* **2015**, *517*, 476–480. [\[CrossRef\]](#)
7. Wehrenfennig, C.; Eperon, G.E.; Johnston, M.B.; Snaith, H.J.; Herz, L.M. High charge carrier mobilities and lifetimes in organolead trihalide perovskites. *Adv. Mater.* **2014**, *26*, 1584. [\[CrossRef\]](#)
8. Baranowski, M.; Plochocka, P. Excitons in metal-halide perovskites. *Adv. Energy Mater.* **2020**, *10*, 1903659. [\[CrossRef\]](#)
9. Lim, J.; Kober-Czerny, M.; Lin, Y.-H.; Ball, J.M.; Sakai, N.; Duijnste, E.A.; Hong, M.J.; Labram, J.G.; Wenger, B.; Snaith, H.J. Long-range charge carrier mobility in metal halide perovskite thin-films and single crystals via transient photo-conductivity. *Nat. Commun.* **2022**, *13*, 4201. [\[CrossRef\]](#)
10. Xu, J.; Maxwell, A.; Wei, M.; Wang, Z.; Chen, B.; Zhu, T.; Sargent, E.H. Defect tolerance of mixed B-site organic–inorganic halide perovskites. *ACS Energy Lett.* **2021**, *6*, 4220–4227. [\[CrossRef\]](#)
11. Zhang, W.; Saliba, M.; Moore, D.T.; Pathak, S.K.; Hörantner, M.T.; Stergiopoulos, T.; Stranks, S.D.; Eperon, G.E.; Alexander-Webber, J.A.; Abate, A. Ultrasoft organic–inorganic perovskite thin-film formation and crystallization for efficient planar heterojunction solar cells. *Nat. Commun.* **2015**, *6*, 6142. [\[CrossRef\]](#) [\[PubMed\]](#)
12. Xiao, M.; Huang, F.; Huang, W.; Dkhissi, Y.; Zhu, Y.; Etheridge, J.; Gray-Weale, A.; Bach, U.; Cheng, Y.B.; Spiccia, L. A fast deposition-crystallization procedure for highly efficient lead iodide perovskite thin-film solar cells. *Angew. Chem. Int. Ed.* **2014**, *53*, 9898–9903. [\[CrossRef\]](#) [\[PubMed\]](#)
13. Pellet, N.; Gao, P.; Gregori, G.; Yang, T.Y.; Nazeeruddin, M.K.; Maier, J.; Grätzel, M. Mixed-organic-cation Perovskite photovoltaics for enhanced solar-light harvesting. *Angew. Chem. Int. Ed.* **2014**, *53*, 3151–3157. [\[CrossRef\]](#) [\[PubMed\]](#)
14. Jeon, N.J.; Noh, J.H.; Kim, Y.C.; Yang, W.S.; Ryu, S.; Seok, S.I. Solvent engineering for high-performance inorganic–organic hybrid perovskite solar cells. *Nat. Mater.* **2014**, *13*, 897–903. [\[CrossRef\]](#) [\[PubMed\]](#)
15. Smith, I.C.; Hoke, E.T.; Solis-Ibarra, D.; McGehee, M.D.; Karunadasa, H.I. A layered hybrid perovskite solar-cell absorber with enhanced moisture stability. *Angew. Chem. Int. Ed.* **2014**, *53*, 11232–11235. [\[CrossRef\]](#)
16. Zhou, Z.; Wang, Z.; Zhou, Y.; Pang, S.; Wang, D.; Xu, H.; Liu, Z.; Padture, N.P.; Cui, G. Methylamine-gas-induced defect-healing behavior of CH<sub>3</sub>NH<sub>3</sub>PbI<sub>3</sub> thin films for perovskite solar cells. *Angew. Chem.* **2015**, *127*, 9841–9845. [\[CrossRef\]](#)
17. Yang, T.Y.; Gregori, G.; Pellet, N.; Grätzel, M.; Maier, J. The significance of ion conduction in a hybrid organic–inorganic lead-iodide-based perovskite photosensitizer. *Angew. Chem.* **2015**, *127*, 8016–8021. [\[CrossRef\]](#)
18. Zhang, H.; Pfeifer, L.; Zakeeruddin, S.M.; Chu, J.; Grätzel, M. Tailoring passivators for highly efficient and stable perovskite solar cells. *Nat. Rev. Chem.* **2023**, *7*, 632–652. [\[CrossRef\]](#)
19. Jaffe, A.; Lin, Y.; Mao, W.L.; Karunadasa, H.I. Pressure-induced metallization of the halide perovskite (CH<sub>3</sub>NH<sub>3</sub>) PbI<sub>3</sub>. *J. Am. Chem. Soc.* **2017**, *139*, 4330–4333. [\[CrossRef\]](#)
20. Lee, J.-Y.; Pandey, P.; Lee, S.; Shen, Q.; Kang, D.-W. Super narrow bandgap (<1.2 eV) halide double perovskites: Recent advancements and future perspectives. *Chem. Eng. J.* **2024**, *491*, 152026. [\[CrossRef\]](#)
21. Xiao, G.; Cao, Y.; Qi, G.; Wang, L.; Liu, C.; Ma, Z.; Yang, X.; Sui, Y.; Zheng, W.; Zou, B. Pressure effects on structure and optical properties in cesium lead bromide perovskite nanocrystals. *J. Am. Chem. Soc.* **2017**, *139*, 10087–10094. [\[CrossRef\]](#) [\[PubMed\]](#)
22. Zhang, Q.; Pei, L.; Li, J.; Wang, K.; Zeng, Q.; Yu, H. Achieving band gap reduction and carrier lifetime enhancement in metal halide perovskites via mechanical stretching. *J. Phys. Chem. Lett.* **2021**, *12*, 7207–7212. [\[CrossRef\]](#) [\[PubMed\]](#)
23. Linaburg, M.R.; McClure, E.T.; Majher, J.D.; Woodward, P.M. Cs<sub>1-x</sub>Rb<sub>x</sub>PbCl<sub>3</sub> and Cs<sub>1-x</sub>Rb<sub>x</sub>PbBr<sub>3</sub> solid solutions: Understanding octahedral tilting in lead halide perovskites. *Chem. Mater.* **2017**, *29*, 3507–3514. [\[CrossRef\]](#)
24. Xiang, W.; Wang, Z.; Kubicki, D.J.; Wang, X.; Tress, W.; Luo, J.; Zhang, J.; Hofstetter, A.; Zhang, L.; Emsley, L. Ba-induced phase segregation and band gap reduction in mixed-halide inorganic perovskite solar cells. *Nat. Commun.* **2019**, *10*, 4686. [\[CrossRef\]](#) [\[PubMed\]](#)
25. Lee, S.; Ryu, J.; Park, S.S.; Yoon, S.; Lee, D.-G.; Moon, J.; Kim, Y.J.; Kang, D.-W. A self-assembled hierarchical structure to keep the 3D crystal dimensionality in n-butylammonium cation-capped Pb–Sn perovskites. *J. Mater. Chem. A* **2021**, *9*, 27541–27550. [\[CrossRef\]](#)
26. Tang, Z.; Bessho, T.; Awai, F.; Kinoshita, T.; Maitani, M.M.; Jono, R.; Murakami, T.N.; Wang, H.; Kubo, T.; Uchida, S. Hysteresis-free perovskite solar cells made of potassium-doped organometal halide perovskite. *Sci. Rep.* **2017**, *7*, 12183. [\[CrossRef\]](#)
27. Lee, S.; Kang, D.-W. Highly efficient and stable Sn-rich perovskite solar cells by introducing bromine. *ACS Appl. Mater. Interfaces* **2017**, *9*, 22432–22439. [\[CrossRef\]](#)
28. Li, C.; Wei, J.; Sato, M.; Koike, H.; Xie, Z.-Z.; Li, Y.-Q.; Kanai, K.; Kera, S.; Ueno, N.; Tang, J.-X. Halide-substituted electronic properties of organometal halide perovskite films: Direct and inverse photoemission studies. *ACS Appl. Mater. Interfaces* **2016**, *8*, 11526–11531. [\[CrossRef\]](#)
29. Zhao, B.; Abdi-Jalebi, M.; Tabachnyk, M.; Glass, H.; Kamboj, V.S.; Nie, W.; Pearson, A.J.; Puttison, Y.; Gödel, K.C.; Beere, H.E. High open-circuit voltages in tin-rich low-bandgap perovskite-based planar heterojunction photovoltaics. *Adv. Mater.* **2017**, *29*, 1604744. [\[CrossRef\]](#)
30. Lee, S.; Moon, J.; Ryu, J.; Parida, B.; Yoon, S.; Lee, D.-G.; Cho, J.S.; Hayase, S.; Kang, D.-W. Inorganic narrow bandgap CsPb<sub>0.4</sub>Sn<sub>0.6</sub>I<sub>2</sub>. 4Br<sub>0.6</sub> perovskite solar cells with exceptional efficiency. *Nano Energy* **2020**, *77*, 105309. [\[CrossRef\]](#)
31. Lau, C.F.J.; Zhang, M.; Deng, X.; Zheng, J.; Bing, J.; Ma, Q.; Kim, J.; Hu, L.; Green, M.A.; Huang, S. Strontium-doped low-temperature-processed CsPbI<sub>2</sub>Br perovskite solar cells. *ACS Energy Lett.* **2017**, *2*, 2319–2325. [\[CrossRef\]](#)

32. Akkerman, Q.A.; Meggiolaro, D.; Dang, Z.; De Angelis, F.; Manna, L. Fluorescent alloy  $\text{CsPb}_x\text{Mn}_{1-x}\text{I}_3$  perovskite nanocrystals with high structural and optical stability. *ACS Energy Lett.* **2017**, *2*, 2183–2186. [\[CrossRef\]](#) [\[PubMed\]](#)
33. Zou, S.; Liu, Y.; Li, J.; Liu, C.; Feng, R.; Jiang, F.; Li, Y.; Song, J.; Zeng, H.; Hong, M. Stabilizing cesium lead halide perovskite lattice through Mn (II) substitution for air-stable light-emitting diodes. *J. Am. Chem. Soc.* **2017**, *139*, 11443–11450. [\[CrossRef\]](#) [\[PubMed\]](#)
34. Xiong, Y.; Xu, L.; Wu, P.; Sun, L.; Xie, G.; Hu, B. Bismuth doping-induced stable seebeck effect based on  $\text{MAPbI}_3$  polycrystalline thin films. *Adv. Funct. Mater.* **2019**, *29*, 1900615. [\[CrossRef\]](#)
35. Hu, Y.; Qiu, T.; Bai, F.; Miao, X.; Zhang, S. Enhancing moisture-tolerance and photovoltaic performances of  $\text{FAPbI}_3$  by bismuth incorporation. *J. Mater. Chem. A* **2017**, *5*, 25258–25265. [\[CrossRef\]](#)
36. Yavari, M.; Ebadi, F.; Meloni, S.; Wang, Z.S.; Yang, T.C.-J.; Sun, S.; Schwartz, H.; Wang, Z.; Niesen, B.; Durantini, J. How far does the defect tolerance of lead-halide perovskites range? The example of Bi impurities introducing efficient recombination centers. *J. Mater. Chem. A* **2019**, *7*, 23838–23853. [\[CrossRef\]](#)
37. Kundu, S.; Zhang, D.; Askar, A.M.; Moloney, E.G.; Adachi, M.M.; Nadeem, A.; Moradi, S.; Yeddu, V.; Abdelhady, A.L.; Voznyy, O. Bismuth stabilizes the  $\alpha$ -phase of formamidinium lead iodide perovskite single crystals. *ACS Mater. Lett.* **2022**, *4*, 707–712. [\[CrossRef\]](#)
38. Hu, Y.; Bai, F.; Liu, X.; Ji, Q.; Miao, X.; Qiu, T.; Zhang, S. Bismuth incorporation stabilized  $\alpha$ - $\text{CsPbI}_3$  for fully inorganic perovskite solar cells. *ACS Energy Lett.* **2017**, *2*, 2219–2227. [\[CrossRef\]](#)
39. Kajal, S.; Kim, J.; Shin, Y.S.; Singh, A.N.; Myung, C.W.; Kim, J.Y.; Kim, K.S. Unfolding the influence of metal doping on properties of  $\text{CsPbI}_3$  perovskite. *Small Methods* **2020**, *4*, 2000296. [\[CrossRef\]](#)
40. Wang, G.; Cheng, L.; Bi, J.; Chang, J.; Meng, F. B-site doping with bismuth ion enhances the efficiency and stability of inorganic  $\text{CsSnI}_3$  perovskite solar cell. *Mater. Lett.* **2024**, *354*, 135394. [\[CrossRef\]](#)
41. Lee, M.; Yoo, B.; Im, J.; Hyeon, T.; Chung, I. Electronic band engineering via  $\text{MI}_3$  ( $\text{M} = \text{Sb}, \text{Bi}$ ) doping remarkably enhances the air stability of perovskite  $\text{CsSnI}_3$ . *ACS Appl. Energy Mater.* **2020**, *3*, 10477–10484. [\[CrossRef\]](#)
42. Tauc, J. *Amorphous and Liquid Semiconductors*; Springer Science & Business Media: Berlin/Heidelberg, Germany, 2012.
43. Lehner, A.J.; Fabiani, D.H.; Evans, H.A.; Hébert, C.-A.; Smock, S.R.; Hu, J.; Wang, H.; Zwaniger, J.W.; Chabiny, M.L.; Seshadri, R. Crystal and electronic structures of complex bismuth iodides  $\text{A}_3\text{Bi}_2\text{I}_9$  ( $\text{A} = \text{K}, \text{Rb}, \text{Cs}$ ) related to perovskite: Aiding the rational design of photovoltaics. *Chem. Mater.* **2015**, *27*, 7137–7148. [\[CrossRef\]](#)
44. Park, B.-W.; Philippe, B.; Zhang, X.; Rensmo, H.; Boschloo, G.; Johansson, E. Bismuth Based Hybrid Perovskites  $\text{A}_3\text{Bi}_2\text{I}_9$  ( $\text{A}$ : Methylammonium or Cesium) for Solar Cell Application. *Adv. Mater.* **2015**, *27*, 6806–6813. [\[CrossRef\]](#) [\[PubMed\]](#)
45. Saparov, B.; Hong, F.; Sun, J.-P.; Duan, H.-S.; Meng, W.; Cameron, S.; Hill, I.G.; Yan, Y.; Mitzi, D.B. Thin-film preparation and characterization of  $\text{Cs}_3\text{Sb}_2\text{I}_9$ : A lead-free layered perovskite semiconductor. *Chem. Mater.* **2015**, *27*, 5622–5632. [\[CrossRef\]](#)
46. Wang, L.; Chen, P.; Kuttipillai, P.S.; King, I.; Staples, R.; Sun, K.; Lunt, R.R. Epitaxial stabilization of tetragonal cesium tin iodide. *ACS Appl. Mater. Interfaces* **2019**, *11*, 32076–32083. [\[CrossRef\]](#)
47. Zhang, J.; Yu, C.; Wang, L.; Li, Y.; Ren, Y.; Shum, K. Energy barrier at the N719-dye/ $\text{CsSnI}_3$  interface for photogenerated holes in dye-sensitized solar cells. *Sci. Rep.* **2014**, *4*, 6954. [\[CrossRef\]](#)
48. Lee, B.; Stoumpos, C.C.; Zhou, N.; Hao, F.; Malliakas, C.; Yeh, C.-Y.; Marks, T.J.; Kanatzidis, M.G.; Chang, R.P. Air-stable molecular semiconducting iodosalts for solar cell applications:  $\text{Cs}_2\text{SnI}_6$  as a hole conductor. *J. Am. Chem. Soc.* **2014**, *136*, 15379–15385. [\[CrossRef\]](#)
49. Saparov, B.; Sun, J.-P.; Meng, W.; Xiao, Z.; Duan, H.-S.; Gunawan, O.; Shin, D.; Hill, I.G.; Yan, Y.; Mitzi, D.B. Thin-film deposition and characterization of a Sn-deficient perovskite derivative  $\text{Cs}_2\text{SnI}_6$ . *Chem. Mater.* **2016**, *28*, 2315–2322. [\[CrossRef\]](#)
50. Qiu, X.; Cao, B.; Yuan, S.; Chen, X.; Qiu, Z.; Jiang, Y.; Ye, Q.; Wang, H.; Zeng, H.; Liu, J. From unstable  $\text{CsSnI}_3$  to air-stable  $\text{Cs}_2\text{SnI}_6$ : A lead-free perovskite solar cell light absorber with bandgap of 1.48 eV and high absorption coefficient. *Sol. Energy Mater. Sol. Cells* **2017**, *159*, 227–234. [\[CrossRef\]](#)
51. Zhang, Z.; Ren, L.; Yan, H.; Guo, S.; Wang, S.; Wang, M.; Jin, K. Bandgap narrowing in Bi-doped  $\text{CH}_3\text{NH}_3\text{PbCl}_3$  perovskite single crystals and thin films. *J. Phys. Chem. C* **2017**, *121*, 17436–17441. [\[CrossRef\]](#)
52. Abdelhady, A.L.; Saidaminov, M.I.; Murali, B.; Adinolfi, V.; Voznyy, O.; Katsiev, K.; Alarousu, E.; Comin, R.; Dursun, I.; Sinatra, L. Heterovalent dopant incorporation for bandgap and type engineering of perovskite crystals. *J. Phys. Chem. Lett.* **2016**, *7*, 295–301. [\[CrossRef\]](#) [\[PubMed\]](#)
53. Wang, R.; Zhang, X.; He, J.; Ma, C.; Xu, L.; Sheng, P.; Huang, F.  $\text{Bi}^{3+}$ -doped  $\text{CH}_3\text{NH}_3\text{PbI}_3$ : Red-shifting absorption edge and longer charge carrier lifetime. *J. Alloys Compd.* **2017**, *695*, 555–560. [\[CrossRef\]](#)
54. Ouyang, R. Exploiting ionic radii for rational design of halide perovskites. *Chem. Mater.* **2019**, *32*, 595–604. [\[CrossRef\]](#)

**Disclaimer/Publisher's Note:** The statements, opinions and data contained in all publications are solely those of the individual author(s) and contributor(s) and not of MDPI and/or the editor(s). MDPI and/or the editor(s) disclaim responsibility for any injury to people or property resulting from any ideas, methods, instructions or products referred to in the content.